

Monitoring Tumor Growth and Treatment in Small Animals with Magnetic Resonance and Optical Tomographic Imaging

J. Masciotti^{a*}, F. Provenzano^a, J. Papa^c, A. Klose^a, J. Hur^a, X. Gu^a, D. Yamashiro^c,
J. Kandel^c, A. H. Hielscher^{a,b*}

^aDept. Biomedical Engineering, Columbia University, 500 West 120th Street New York, NY 10027

^bDept. Radiology, Columbia University, 660 West 168th Street, New York, NY 10032

^cDept. Surgery, Columbia University, 3959 Broadway, New York, NY 10032

ABSTRACT

Small animal models are employed to simulate disease in humans and to study its progression, what factors are important to the disease process, and to study the disease treatment. Biomedical imaging modalities such as magnetic resonance imaging (MRI) and Optical Tomography make it possible to non-invasively monitor the progression of diseases in living small animals and study the efficacy of drugs and treatment protocols. MRI is an established imaging modality capable of obtaining high resolution anatomical images and along with contrast agents allow the studying of blood volume. Optical tomography, on the other hand, is an emerging imaging modality, which, while much lower in spatial resolution, can separate the effects of oxyhemoglobin, deoxyhemoglobin, and blood volume with high temporal resolution. In this study we apply these modalities to imaging the growth of kidney tumors and then their treatment by an anti-VEGF agent. We illustrate how these imaging modalities have their individual uses, but can still supplement each other and cross validation can be performed.

Keywords: Optical Tomography, Small animal Imaging, MRI, Multimodality Imaging, VEGF

1. INTRODUCTION

Advances in animal models of human disease and the desire to non-invasively monitor the spatial and temporal progression of disease and other biological processes have motivated recent interest in and development of small animal imaging systems^{1,2,3,4}. Magnetic resonance imaging and Optical Tomographic Imaging are two modalities that show promise in this regard. MRI is an established imaging modality capable of obtaining high resolution anatomical images⁵ as well as studying cerebral blood volume⁶ (CBV), cerebral blood flow (CBF), and cerebral metabolic rate of oxygen (CMRO₂). It allows monitoring anatomical changes such as tumor growth and regression, though it is insensitive to some physiological changes. Optical tomography, on the other hand, is an emerging imaging modality, which, while much lower in spatial resolution than MRI and insensitive to CBF, can be used to measure physiologically important chromophore concentrations such as oxyhemoglobin (HbO₂) and deoxyhemoglobin (Hb) with high temporal resolution^{7,8,9,10,11}. Furthermore, optical methods are also sensitive to scattering properties, blood volume changes and can be used in combination with molecular markers^{12,13,14}. Dynamic, functional imaging can be performed with temporal resolution in the range of 1 Hz to 35 Hz¹⁵. One promising application is the monitoring of hemodynamic effects during cancer treatment in mouse models. For example, we have used optical tomography combined with MRI to monitor regression of tumors in mice after treatment with a vascular endothelial growth factor (VEGF) antagonist¹⁶. We found that reduction in blood volume can be observed as early as 24 hours after treatment, when anatomical changes are not yet visible in MR images. This finding was in agreement with other studies that have shown disrupting VEGF signaling, which is responsible for angiogenesis, and can attenuate or even abolish tumor vasculature, producing marked tumor regression^{17,18,19,20,21}. It is not well understood what causes the destruction of blood vessels in the tumor which leads to its regression. Here, the early onset of the drug-tissue interaction is of special interest. In this study we use MRI to monitor tumor growth and then use Optical Tomography to monitor the physiological changes that occur immediately and within 24 hours after treatment.

* Corresponding authors' emails: James Masciotti: (jmm2014@columbia.edu), Andreas H. Hielscher: (ahh2004@columbia.edu)

2. METHODS

2.1 Mouse Model for Pediatric Tumor

We studied the growth and regression of Wilms tumors implanted in the kidneys of NCR athymic nude mice. One of the goals of this study was to judge the efficacy of an anti-VEGF treatment. VEGF (vascular endothelial growth factor) is a polypeptide that is secreted by cells and acts as a mitogen for vascular endothelial cells and stimulates the formation of new blood vessels, a process called angiogenesis. Effective anti-VEGF therapies block the action of VEGF and



Figure 1: Left Mouse Kidney with tumor (left), and normal kidney (right)

prevent the growth of new blood vessels in the tumor. They can even destabilize the newly formed blood vessels and cause tumor regression. It has been shown in several animal studies that disruption of VEGF signaling can attenuate or even abolish tumor vasculature, producing marked tumor regression. VEGF blockade has recently been validated as a therapeutic strategy in clinical trials, leading to the approval of the anti-VEGF antibody bevacizumab (Avastin®) by the FDA in February 2004. In this study, tumor cells were injected into the left kidney of 10 mice and allowed to grow undisturbed, for 30 days. Two mice were not injected with tumor cells and were used as controls. In order to judge the potential for monitoring tumor growth in the mouse tumor model, mice were imaged every 7 days with MRI and twice every seven days with Optical Tomography for a length of 22 days. On the 52nd day after implantation, a treatment schedule consisting of two injections a week was begun. Fig. 1 shows how a mouse kidney with tumor (left) compares to a healthy kidney (right).

2.2 Magnetic Resonance Imaging

Magnetic Resonance Imaging was performed with a 9.4T magnet and a Bruker Avance 400 spectrometer equipped with a Bruker micro2.5 imaging gradient, Fig. 2 (left). A linear polarized RF birdcage coil insert, Fig. 2 (right), 3.8 cm in

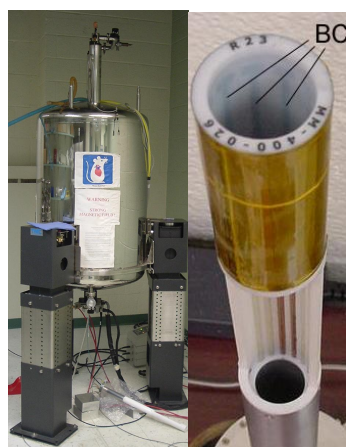


Figure 2: Bruker 9.4T Instrument (left) and RF birdcage coil (right)

outer diameter, was inserted into the gradient set. There was a 3 cm diameter space in the coil for the animal holder which provided 2.5cm diameter for the animal to be secured for imaging. Two tuning and matching capacitors allowed the RF coil to be tuned to the lamour frequency of 400 MHz. Prior to scanning, mice were anesthetized with 1.5% isoflourane and a PE-10 size catheter was inserted into the peritoneal cavity. A syringe filled with .7cc of 50 μ M gadodiamide (Omniscan) was inserted to the distal side of the catheter. The MRI scanning protocol consisted of first adjusting the position of the animal in the scanner, with triplanar MSME scout scans, so that the tumor or kidneys were in the center of the scanning volume (20 minutes average). Then, shimming was performed and spectrometer parameters were adjusted (5 minutes). Then, a T2 weighted fast spin echo scan²², followed by gradient echo scan²³ were acquired (30 minutes each). The contrast agent was then injected and 15 minutes was allowed for the contrast agent to reach steady state in the blood stream. Finally, post contrast fast spin echo and gradient echo scans were acquired (30 minutes each). Fast spin echo scans were performed with a repetition time TR = 3.125 ms, and echo time TE = 31.9 ms, a RARE factor of 6, and the number of acquisitions Nex was 10. The gradient echo scans had a repetition time TR = 725 ms, an echo time of 8 ms, and the number of acquisitions Nex was 10. There

were 30 slices each with a separation of 0.85 mm, and a slice area of 2.56 cm x 2.56 cm. The fast spin echo images were reconstructed with a matrix size of 512 x 512, while the gradient echo images were reconstructed with a matrix size of 256 x 256.

In brain imaging, MRI can allow the use of blood pool contrast agents to produce physiologically informative maps of blood volume and microvasculare density²⁴. In small animal MRI studies, the contrast agent is usually administered while the animal is inside the imaging apparatus and is done so through an intravenous or intraperitoneal cavity catheter and the contrast agent reaches steady state in 15 minutes or less. One can use pre and post contrast scans to calculate the

contrast agent induced shift in the transverse relaxation rates R_2 , R_2^* which is proportional to the blood pool contrast agent concentration ,CA, and thus the blood volume density as given by (1).

$$BV \propto [CA] \propto (\Delta R_2 \text{ or } \Delta R_2^*) = \left(\frac{1}{TE} \right) \ln \left(\frac{S_{pre}}{S_{post}} \right) \quad (1)$$

The pre and post contrast spin echo and gradient echo scans will be used to compute Blood volume maps for the tumor. The pre-contrast spin echo images will also be used for their anatomical information.

2.3 Optical Tomographic Imaging

For this study, a continuous wave dynamic near-infrared optical tomographic (DYNOT)²⁵ was used. Laser light at 2 wavelengths (wavelengths $\lambda_1 = 760$ and $\lambda_2 = 830$ nm) is delivered to up to 24 source fiber bundles via an optical demultiplexing switch which allow light to be sequential delivered to different positions. The demultiplexor consists of a mirror mounted on a rotating stepper motor which reflects light from the incoming laser sources into different source fibers based on the angular orientation of the mirror. Up to 32 detector fiber bundles are used to direct light to detector cards. Light is incident onto silicon photodiodes, which are connected to a series of programmable amplifiers and a lock-in filter. Since the amount of light a given detector collects will vary greatly depending on the position of the source that is illuminated, variable gain setting are implemented on the programmable gain amplifiers. Their adjustment is synchronized with the switching of the sources. More details concerning the system can be found in ref. The optical imaging probe consisted of a 5 cm diameter cylinder with a height of 10 cm made from white Delrin. Two fiber holding rings machined from black Delrin allow the ends of the fiber bundles to be in direct contact with the cylinder. Each ring had 24 holes drilled, angularly space 15° apart, allowing 12 source and 12 detector fiber bundles to be connected to each rings in an alternating pattern. We used a total of 24 sources and 24 detectors giving us 576 source detector pairs for each tomographic data set. The rings can also be slid up and down to adjust the vertical position of the imaging planes. Mice were lowered into the imaging probe by an arm of a stereotaxic frame. The mouse was positioned so that the tumor was located in between to two rings which were separated by 2 cm. 1% Intralipid was used as a matching fluid in order to reduce edge effects during reconstructions and to ensure that the propagation of light into the tissue can be correctly modeled by our reconstruction algorithms. The scan rate of the instrument was 2.5 Hz which meant that a full tomographic data set was collected every 400 ms. Two types of scans, static and dynamic were performed. For static imaging the mouse was secured in the probe for just under 3 minutes while 400 tomographic data sets were acquired. The measurements would then be averaged in order to improve signal to noise ratio. For dynamic imaging which was performed during the treatment of some animals the mouse was secured in the probe for up to an hour and scanning was done continuously. Subsection of the acquired data would be chosen as 200 point blocks and averaged in order to get a measurement value at a particular time point with sufficient signal to noise ratio.

2.3 Optical Tomographic Reconstruction

In this study, reconstructions of the absorption coefficient were achieved by using frequency domain codes which use a forward model based on the equation of radiative transfer²⁶:

$$\Omega \cdot \nabla \Psi(x, \Omega) + (\mu_a(x) + \mu_s(x)) \Psi(x, \Omega) = \mu_s(x) \int_{4\pi} k(\Omega, \Omega') \Psi(x, \Omega') d\Omega', \quad (2)$$

where ψ is the fluence (W/cm^2), μ_a is the absorption coefficient (cm^{-1}), μ_s is the scattering coefficient (cm^{-1}), Ω is the directional vector, and k describes the probability that photons traveling in direction Ω' are scattered in direction Ω and is given by the Heyney-Greenstein scattering model:

$$k(\cos \theta = \Omega \cdot \Omega') = \frac{1 - g^2}{(1 + g^2 - 2g \cos \theta)^{3/2}}, \quad (3)$$

where g is the anisotropy factor. Equation (2) is often referred to as a forward model, that predicts the detector readings given some approximation of the optical properties μ_a and μ_s . The source term is incorporated in to the boundary conditions:

$$\Psi(\mathbf{x}, \Omega) = S(x, \Omega) \text{ on } \Omega \bullet \mathbf{n}(\mathbf{x}) < 0 \quad (4)$$

Our reconstruction algorithms require the definition of an objective function that determines the discrepancy between measured data M and predicted detector data P generated by the forward model. Because the *DYNOT* instrument does not provide absolute measurements, due to unknown coupling losses in source and detector fibers, a calibration scheme is used that is similar to that suggested by Y. Pei et al²⁷. The calibration scheme requires that the same experimental setup be used to take measurements of the target (mouse) and a homogeneous phantom of known optical properties. We used Intralipid 1% as a phantom which is assumed to have the optical properties^{28,29} in table 1. Intuitively, the calibration scheme can be thought of as using the phantom to find the scaling factors needed to account for unknown losses in each of the source detector pair measurements. According to the calibration scheme, the standard least square norm objective function is modified to yield:

λ (nm)	μ_a (cm ⁻¹)	μ_s (cm ⁻¹)	g
760	.023	27	0.73
830	.027	22	0.71

Table 1: Optical properties assumed for Intralipid 1%

phantom to find the scaling factors needed to account for unknown losses in each of the source detector pair measurements. According to the calibration scheme, the standard least square norm objective function is modified to yield:

$$\Phi(\mu_a, \mu_s, \Psi) = \frac{1}{2} \sum_s \sum_d \frac{\left| \frac{P_{s,d}^{ph} M_{s,d}^m}{M_{s,d}^{ph}} - P_{s,d}^m(\Psi) \right|^2}{\left| \frac{P_{s,d}^{ph} M_{s,d}^m}{M_{s,d}^{ph}} \right|^2} + \frac{\beta}{2} R(\mu_a, \mu_s), \quad (5)$$

where s and d are used for indexing the sources and detectors, Ψ is vector of radiances for all source M^{ph} and M^m are the actual measurements for the phantom and the mouse respectively, P^{ph} and P^m are the forward model predicted measurements for the phantom and target respectively, and R and β are parameters for regularization which is optional.

3. RESULTS

3.1 MRI images of tumor growth

In the first MRI example, shown in Fig. 3, we show anatomical fast spin echo axial images of a mouse without a tumor and a mouse with a tumor implanted on its left kidney. The back is towards the bottom of the images. The back muscles are outlined in red. The spinal cord is the bright area in the center of the back muscles. The healthy kidneys are outline in green. The cancerous kidney and the tumor are outline in yellow. The tumor is located both inside and to the left of the cancerous kidney.

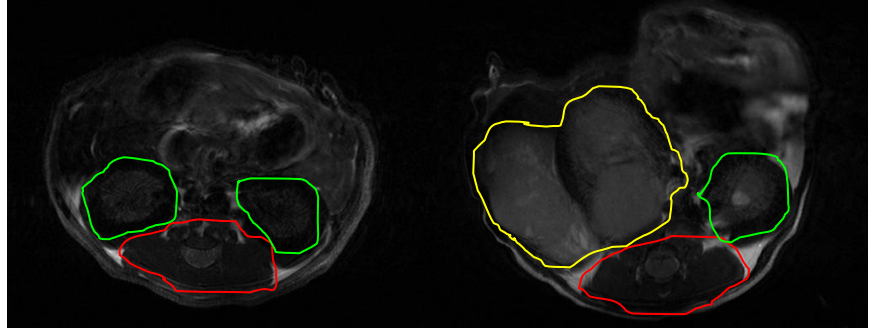


Figure 3: Fast Spin echo image of mouse without (left) and with (right) left kidney tumor. Healthy kidneys (green), back muscles (red), and kidney tumor (yellow) are evident.

In the second example, Fig. 4, we show two mice which have kidney tumors and show how the tumors grown as they have been imaged during successive weeks of a 4 week period.

In both cases, the tumors starts out small, but eventually grow quite large and become a significant part of the mouse itself. In images of mouse 1 (4a – 4d), the tumor begins growing on the surface of the kidney (4a), but then grows into the kidney (4b), overwhelms it and grows quite larger (4c – 4d). In images of mouse 2 (4e – 4h), the tumor starts out small (4e), grows large very quickly (4f – 4g), and eventually takes up the entire abdominal space (4h). In fact the tumors grow so large that, after the 52nd day, the entire volumes that they occupy cannot be covered by the imaging volume of an MRI scan.

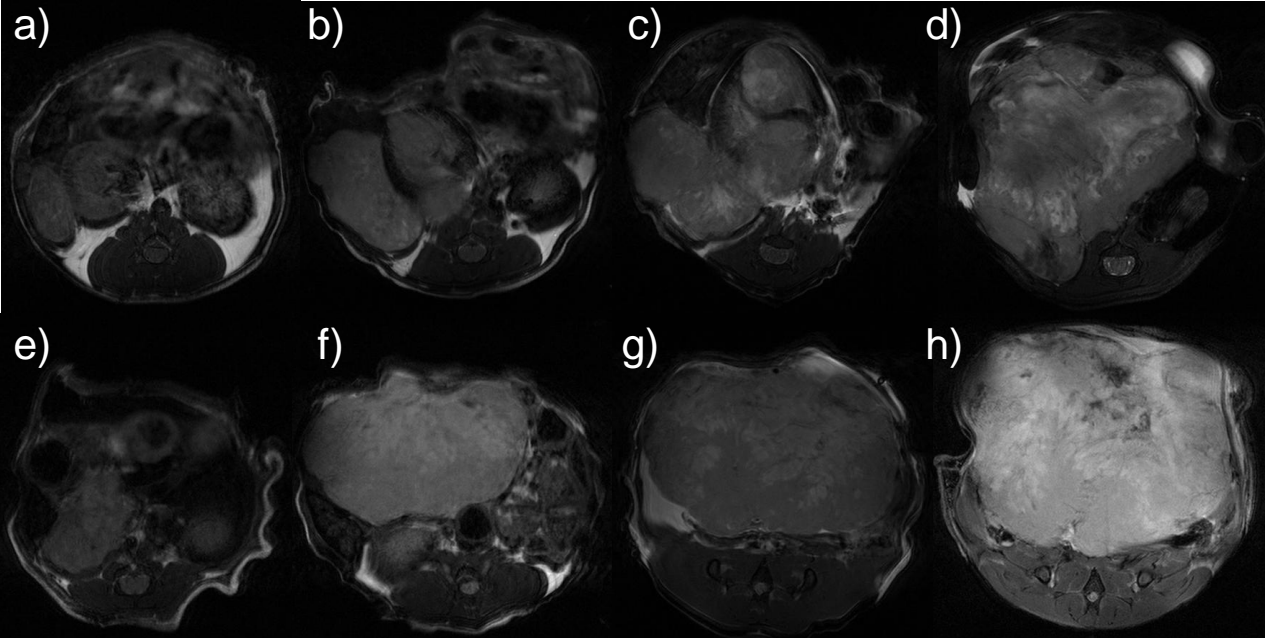


Figure 4: Images of mice for the 31st (a, e), 38th (b,f), 45th (c,g), and 52nd day (d,h) for Mouse 1 (a-d) and Mouse 2 (e – h).

Though these images are 2D slices, images from the whole 3D slice package can be used to calculate the total tumor volume for a better idea of the tumor size. The full 3D data from the mice above were input into a histogram based semi-automated 3D segmentation tool and the resulting volumes were calculated. The resulting plot in Fig. 5 shows that the growth of the tumor in Mouse 1 can be characterized as increasing in size exponentially, while the tumor in Mouse 2 seems to grow fairly linearly with time.

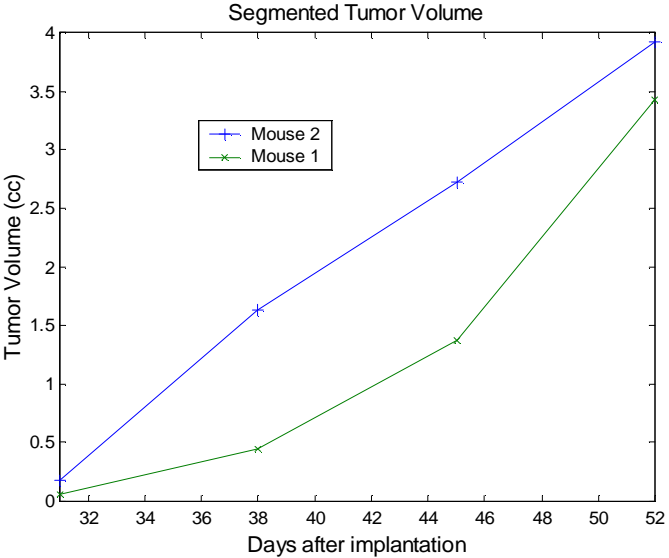


Figure 5: Plot of the segmented tumor volume

Some observations were made concerning the blood volume techniques mentioned in the MRI methods section. In this study tumors grew in the same anatomical space to which the contrast agent was supplied. In this case the contrast agent reached the tumor through direct diffusion in addition to the normal mechanism of vascular perfusion. This

prevented the contrast agent in the tumor from reaching steady state in the same way that it normally does in the brain. In cases where the tumor was large, the contrast agent never reached steady state during the experiment. In cases of a small tumor, the contrast agent appears to have reached steady state in the tumor before the start of the post contrast gradient echo scan. In this case, $\Delta R2^*$ can be used to estimate tumor blood volume density even though $\Delta R2$ can not. The image below in Fig. 6 shows the gradient echo calculated blood volume density overlaid on the tumor area for the same image as in Fig 5a. One can observe there are higher and lower areas of blood volume density in the tumor. The areas of low blood volume might correspond to areas of tissue with low blood perfusion which can become hypoxic or necrotic.

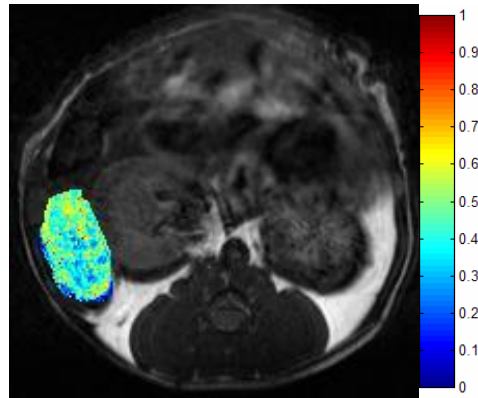


Figure 6: Calculated blood volume density (au) map overlaid on MRI image

3.2 Optical Tomographic Imaging

We have previously shown that optical tomography can be used to monitor the efficacy of cancer drugs in small animals¹⁶. In this study we show 2D axial cross-section reconstructed absorption coefficient maps which we suggest are proportional to the blood volume in the tumor. In the images below in Fig. 7, we show static optical tomographic images of a mouse with a kidney tumor. The images show mouse 1 with a tumor on the 49th (7a), 52nd (7b) and 53rd (7c) day after implantation. In all cases, the area of absorption is in the same area of the mouse, that the MRI images show the tumor to be located. There is a higher absorption coefficient on the 52nd day compared to the 49th day. We believe this is due to an increase in tumor blood volume due to general increase in tumor size. This drastic increase in tumor size can also be seen in the MRI images. In fact, according to Fig. 5, the tumor more than doubles in size between the 45th and 52nd day. The tumor was treated after the scan on the 52nd day. There is lower absorption coefficient on the 53rd day compared to the 52nd day which we believe is due to a decrease in blood volume in the tumor as a result of drug induced blood vessel destruction.

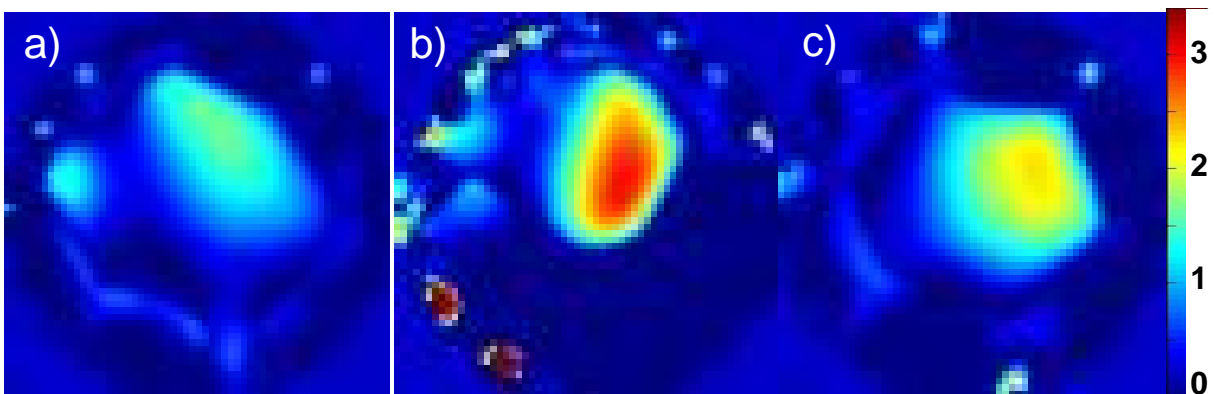


Figure 7: Optical Tomographic images of absorption coefficient μ_a (cm^{-1}) of Mouse 1 on the 49th (a), 52nd (b), and (c) 53rd day.

Dynamic Optical Tomographic images were also taken on the 52nd day after implantation. An example time trace of the measured optical signal for one source detector pair is shown below in Fig. 8. The treatment was administered 4 minutes into the scan at time 0. A small signal decrease occurs from 6 to 9 minutes. A steep sustained signal increase begins just after the dip at 9 minutes and remains for the remainder of the experiment, but becomes more gradual after 20 minutes. The signal decreases and increases in the time trace are most likely due to increases and decreases in absorption respectively.

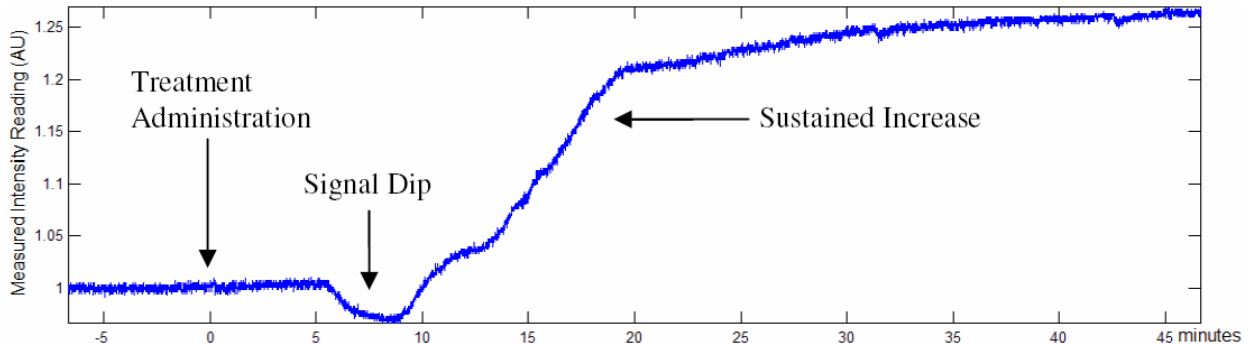


Figure 8: Time trace of measured light intensity for an example source detector pair.

Examples of reconstructed absorption images are presented in Fig. 9. The large circular shape corresponds to the cylinder cross-section. Small areas of high absorption on the edge of the circle are source boundary artifacts. The mouse was located with back against the rear of the cylinder (top of image). Figs. 9a-9e shows the absorption coefficient image for the mouse at various time points from just prior to injection to 32 minutes after injection. The area of high absorption is collocated with the tumor as confirmed with MRI. Figs. (9f-9j) show images that represent the original absorption image (9a) minus the absorption images at each of the various time points. At 8 minutes after drug injection (Figs. 9c and 9h) one can observe a decrease in absorption around the periphery of the tumor and an increase in absorption inside the tumor. A decrease in the absorption coefficient inside the tumor occurs there after. By 32 minutes after injection a large decrease in absorption coefficient is observed inside the tumor. In most cases we observed that this or an even stronger decrease is still present 24 hours after treatment.

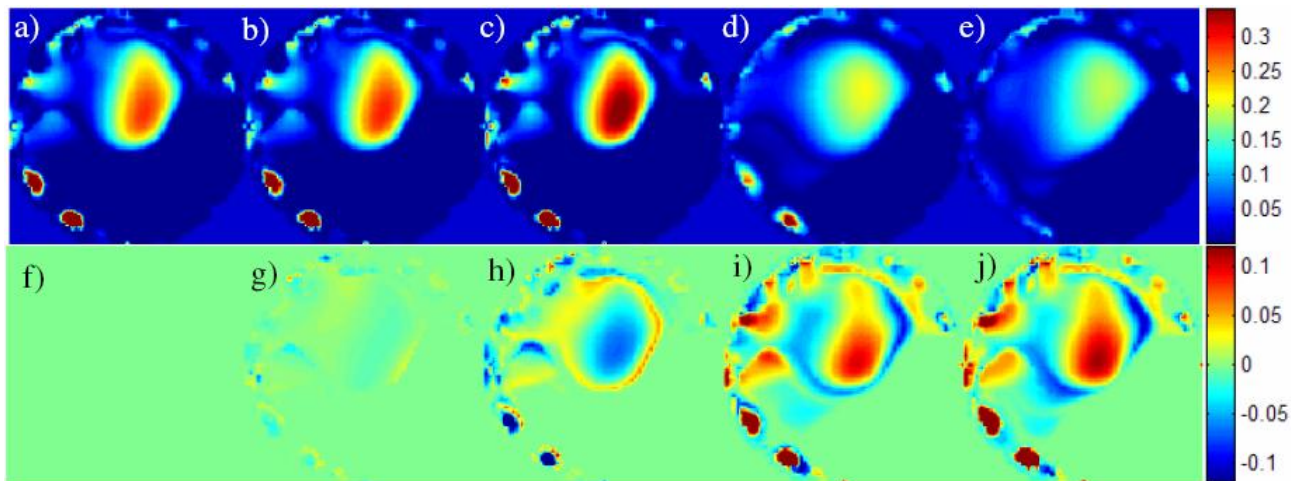


Figure 9: Maps of the absorption coefficient $\mu_a(\text{cm}^{-1})$ for (a) 0, (b) 4, (c) 8, (d) 16, and (e) 32 minutes after injection; and changes in absorption coefficient, with respect to Fig. 11a, for (f) 0, (g) 4, (h) 8, (i) 16, and (j) 32 minutes after injection.

4. CONCLUSIONS

In this study we have imaged kidney-tumor bearing mice with both magnetic resonance imaging and Optical Tomography. MRI provided very useful anatomical information. It also allowed us to closely monitor the growth of the tumors and with the help of segmentation, it allowed us to calculate the size of the tumors at different time points. It did not provide as useful physiological information, however. Because the tumors were located in the same cavity that the contrast agent is delivered, perfusion of the blood pooling contrast agent was complicated by direct contrast agent diffusion into the tumor. This prevented blood volume images from being reconstructed for all cases except for the $\Delta R2^*$ case of the smallest tumor. This problem of contrast agent diffusing into tumors in the peritoneal cavity can be avoided by delivering the contrast agent intravenously, but the lifetime of the contrast agent in the blood will be less than when administered intraperitoneally, and the intravenous catheterization is invasive and cannot be performed repeatedly. Optical tomography can however measure blood volume intrinsically. We have shown how optical tomography can be used to monitor the physiological changes that follow the administration of an anti-VEGF treatment in a tumor bearing mouse. We observed an effect as early as eight minutes after administration of the drug. After a short increase in absorption in the center of the tumor, we observe a sustained decrease in absorption, which we believe corresponds to a decrease in tumor blood volume. We believe this drop in blood volume is most likely due to the fact that blocking VEGF causes a decrease in nitric oxide, which in turn leads to vassal constriction. This immediate decrease in tumor blood volume is different from vascular destruction, which is known to begin 24 hours after treatment, and is known to cause tumor regression. Dual-wavelength studies are currently underway that will allow calculations of changes in Hb and HbO₂ concentration. This information will aid in further understanding of the observed early effects during VEGF antagonist treatment.

ACKNOWLEDGEMENTS

This work was supported in part by the National Institute of Biomedical Imaging and Bioengineering (NIBIB grant number 5R01-EB001900, A. H. Hielscher) and the National Cancer Institute (NCI grant numbers 5R01CA100451, J. Kandel, and 5R01CA088951, D. Yamashiro), which both are divisions of the National Institutes of Health (NIH).

REFERENCES

1. S.R. Cherry, "In vivo molecular imaging and genomic imaging: new challenges for imaging physics," *Phys. Med. Biol.* **49**, R13 (2004).
2. M. G. Pomper, "Can small animal imaging accelerate drug development?" *Journal Cellular Biochemistry Suppl.* **39**, pp. 211-220. (2002).
3. P. D. Acton, H. F. Kung, "Small animal imaging with high resolution single photon emission tomography," *Nuclear Medicine and Biology* **30**(8), pp. 889-895 (2003).
4. D. M. McDonald, P. L. Choyke, "Imaging of angiogenesis: from microscope to clinic," *Nature Medicine* **9**(6), 713-725 (2003).
5. G. A. Johnson, G. P. Cofer, B. Fubara, S. L. Gewalt, L. W. Hedlund, R. R. Maronpot, "Magnetic resonance histology for morphologic phenotyping," *Journal of Magnetic Resonance Imaging* **16**(4), pp. 423-429 (2002).
6. E. X. Wu, K. K. Wong, M. Andrassy, H. Tang, "High-resolution in vivo CBV mapping with MRI in wild-type mice," *Magnetic Resonance in Medicine* **49**(4), pp. 765-770 (2003).
7. A.H. Hielscher, "Optical tomographic imaging of small animals," *Current Opinion in Biotechnology* **16**(1), pp. 79-88 (2005).
8. A. Y. Bluestone, M. Stewart, B. Lei, I.S. Kass, J. Lasker, G.S. Abdoulaev, A. H. Hielscher, "Three-dimensional optical tomographic brain imaging in small animals, Part I: Hypercapnia," *Journal of Biomedical Optics* **9**(5), pp. 1046-1062 (2004).
9. A. Y. Bluestone, M. Stewart, J. Lasker, G.S. Abdoulaev, A. H. Hielscher, "Three-dimensional optical tomographic brain imaging in small animals, Part II: Unilateral Carotid Occlusion," *Journal of Biomedical Optics* **9**(5), pp. 1063-1073 (2004).
10. J. P. Culver, T. Durduran, D. Furuya, C. Cheung, J. H. Greenberg, A. G. Yodh, "Diffuse optical tomography of cerebral blood flow, oxygenation, and metabolism in rat during focal ischemia," *Journal of Cerebral Blood Flow & Metabolism* **23** pp. 911-924 (2003).
11. G. Yu, T. Durduran, D. Furuya, J. H. Greenberg, A. G. Yodh, "Frequency-domain multiplexing system for in vivo diffuse light measurements of rapid cerebral hemodynamics," *Applied Optics* **42**(16), pp. 2931-2939 (2003).
12. E. E. Graves, R. Weissleder, V. Ntziachristos, "Fluorescence Molecular Imaging of Small Animal Tumor Models," *Current Molecular Medicine* **4**, pp. 419-430 (2004).
13. M. Doubrovin, I. Serganova, P. Mayer-Kuckuk, V. Ponomarev, R. G. Blasberg, "Multimodality in Vivo Molecular-Genetic Imaging," *Bioconjugate Chemistry* **15**, pp.1376-1388 (2004).

-
14. V. Ntziachristos, E. A. Schellenberger, J. Ripoll, D. Yessayan, E. Graves, A. Bodganov, L. Josephson, R. Weissleder, "Visualization of antitumor treatment by means of fluorescence molecular tomography with an annexin V-Cy5.5 conjugate," *Proceedings of the National Academy of Science of the United States of America* **101**(33), pp. 12294-12299 (2004).
 15. D. Piao, S. Jiang, S. Srinivasan, H. Dehgani, B. Pogue, "Video-rate near-infrared optical tomography using spectrally encoded parallel light delivery," *Optics Letters* **30**(19), pp. 2593-2595 (2005).
 16. J. Masciotti, G. Abdoulaev, J. Hur, J. Papa, J. Bae, J. Huang, D. Yamashiro, J. Kandel, A.H. Hielscher, "Combined optical tomographic and magnetic resonance imaging of tumor bearing mice," in *Optical Tomography and Spectroscopy of Tissue VII*, B. Chance, R.R. Alfano, B.J. Tromberg, M. Tamura, E.M. Sevick-Muraca, eds., Proc. 5693, pp. 74-81 (2005).
 17. H. P. Gerber, J. Kowalski, D. Sherman, D. A. Eberhard, N. Ferrara, "Complete Inhibition of Rhabdomyosarcoma Xenograft Growth and Neovascularization Requires Blockade of Both Tumor and Host Vascular Endothelial Growth Factor," *Cancer Research* **60**, pp. 6253-6258 (2000).
 18. M. Prewett, J. Huber, Y. Li, A. Santiago, W. O'Connor, K. King, J. Overholser, A. Hooper, B. Pytowski, L. Witte, *et al*, "Antivascular Endothelial Growth Factor Receptor (Fetal Liver Kinase 1) Monoclonal Antibody Inhibits Tumor Angiogenesis and Growth of Several Mouse and Human Tumors," *Cancer Res.* **59**, pp. 5209-5218 (1999).
 19. J. Glade-Bender, J. J. Kandel, D. J. Yamashiro, "VEGF blocking therapy in the treatment of cancer," *Expert Opinion on Biological Therapy* **3**(2), pp. 263-276 (2003).
 20. J. Z. Huang, J. S. Frischer, A. Serur, A. Kadenhe, A. Yokoi, K. W. McCrudden, T. New, K. O'Toole, S. Zabski, J. S. Rudge, J. Holash, G. D. Yancopoulos, D. J. Yamashiro, J. J. Kandel, "Regression of established tumors and metastases by potent vascular endothelial growth factor blockade," *Proceedings of the National Academy of Science of the United States of America* **100**(13), pp. 7785-7790 (2003).
 21. J. S. Frischer, J. Z. Huang, A. Serur, A. Kadenhe-Chiweshe, K. W. McCrudden, K. O'Toole, J. Holash, G. D. Yancopoulos, D. J. Yamashiro, J. J. Kandel, "Effects of potent VEGF blockade on experimental Wilms tumor and its persisting vasculature," *International Journal of Oncology* **25**(3), pp. 549-553 (2004).
 22. J. Hennig, A. Nauwerth, H. Friedburg, "RARE imaging: a fast imaging method for clinical MR," *Magnetic Resonance in Medicine*, **3**(6), pp. 823-833 (1986).
 23. A. Haase, J. Frahm, D. Mattaei, W. Haenicke, K. Merboldt, "FLASH imaging, rapid NMR imaging using low flip-angle pulses," *Journal of Magnetic Resonance* **67**(2), pp 258-266 (1986).
 24. E. Wu, H. Tang, J. Jensen, "Applications of ultrasmall superparamagnetic iron oxide contrast agents in the MR study of animal models," *NMR in Biomedicine* **17**(7), pp. 478-483 (2004).
 25. C.H. Schmitz, M. Löcker, J. M. Lasker, A. H. Hielscher, R. L. Barbour, "Instrumentation for fast functional optical tomography," *Review of Scientific Instrumentation* **73**(2), pp. 429-439 (2002).
 26. A. K. Klose, V. Ntziachristos, A. H. Hielscher, "The inverse source problem based on the radiative transfer equation in molecular imaging," *Journal of Computational Physics* **202** pp. 323-345 (2005).
 27. Y. Pei, H. L. Graber, and R. L. Barbour: Influence of systematic errors in reference states on image quality and on stability of derived information for DC optical imaging, *Applied Optics* **40**, 5755-5769 (2001).
 28. S. T. Flock, S. L. Jacques, B. C. Wilson, W. M. Star, M. J. C. van Gemrt, "Optical Properties of Intralipid: A phantom medium for light propagation studies," *Lasers in Surgery and Medicine* **12**(5) pp. 510-519 (1992).
 29. H. G. Staveren, C. J. M. Moes, J. van Marle, S. A. Prahl, M. J. C. van Gemert, "Light scattering in Intralipid-10% in the wavelength range of 400 -1100 nanometers," *Applied Optics* **30**(31) pp. 4507-4514 (1991).